C. R. Mecanique 339 (2011) 756–769

Contents lists available at SciVerse ScienceDirect

Comptes Rendus Mecanique

www.sciencedirect.com

Soot and radiation modeling in laminar ethylene flames with tabulated detailed chemistry

Luc-Henry Dorey [a,*], Nicolas Bertier [a], Lionel Tessé [a], Francis Dupoirieux [b]

[a] Onera – The French Aerospace Lab, 29, avenue de la Division Leclerc, 92322 Châtillon cedex, France
[b] Onera – The French Aerospace Lab, 91761 Palaiseau cedex, France

ARTICLE INFO

Article history:
Received 25 May 2011
Accepted after revision 14 September 2011
Available online 4 October 2011

Keywords:
Combustion
Soot modeling
Radiative transfer modeling
Sooting flames
Tabulated chemistry

ABSTRACT

A strategy has been developed in order to compute unsteady convective and radiative heat transfers in an industrial combustion device. This strategy involves a tabulation method to describe gas-phase chemistry, coupled with a semi-empirical soot model. A Monte Carlo method is used to evaluate gas and soot radiative transfer. This paper presents the first validation step of this strategy, in which four laminar premixed ethylene flames have been simulated. The tabulation method well predicts gas-phase species concentrations, including acetylene, considered as the main soot precursor. The soot model gives results in the experimental uncertainty range of measurements, whereas radiative powers highlight the dominating role of soot particles.

1. Introduction

To conform to more and more stringent pollutant emission rules, regarding in particular nitrogen oxides (NO_x) and soot levels, new combustion chambers have to be designed. Soot particles influence combustion and thermal conditions inside gas turbine combustion chambers, because they may strongly enhance the radiative transfer, that reduces the maximum gas temperature and consequently affect the temperature-dependent NO_x formation. Radiative transfer also increases the wall heat load, which tends to decrease the wall material lifetime. Therefore, soot are undesired products and the modeling of their formation and radiation has to be taken into account in simulations of industrial combustors. Very recent studies [1,2] highlight the need for accurate and affordable soot and radiation models in industrial CFD (Computational Fluid Dynamics) codes, i.e. which are able to treat unstructured meshes and turbulent compressible reactive flows. Moreover, simulations of gas turbine chambers have demonstrated in the past few years that Large Eddy Simulation (LES) provides more accurate results than those given by the RANS (Reynolds-Averaged Navier–Stokes) approach (see e.g. Boudier et al. [3]), and well captures combustion instabilities and ignition process [4,5]. Consequently, the aim of the study presented in this paper is to develop a methodology which is able to compute unsteady combustion with soot formation coupled with radiative transfer in practical combustion devices.

Soot formation modeling is a difficult and challenging task. Involved processes differ from those implicated in the formation of chemical species, because they include longer characteristic time and heterogeneous phase reactions. The need for predictive models in various conditions of combustion, at different levels of pressure and using different fuels has driven the work on soot modeling during the last fifty years (see for example the recent paper of Wang [6]). Although some sooting phenomena are still not explained, numerous models with different levels of complexity have been elaborated and presented below.

* Corresponding author.
E-mail address: Luc-Henry.Dorey@onera.fr (L.-H. Dorey).

1631-0721/$ – see front matter
doi:10.1016/j.crme.2011.09.004

Detailed complex kinetic schemes [7,8] have been developed in order to investigate soot kinetic processes in laminar flames. They describe detailed chemical phenomena such as fuel pyrolysis and oxidation, and formation of soot precursors: acetylene, benzene and PAHs (Polycyclic Aromatic Hydrocarbons). To that end, they involve about a hundred species and hundreds of reactions. Such detailed schemes were combined with a detailed sectional dynamics model and a PAH-based soot model to describe the soot Particle-Size Distribution Function (PSDF) in flames, as realized by D'Anna et al. [9] in the laminar diffusion flame of Santoro et al. [10]. Recently, this approach allowed Zhang et al. [11] to investigate in the same flame soot particle dynamics in details, focusing on the role of aggregate coagulation efficiency, and exploring still not well understood phenomena such as the particle coalescence process. However, these detailed models are restricted to simple laboratory flame simulations, because of their high computation costs induced by the treatment of one hundred of species and up to 35 sections.

Some modeling efforts have been made on soot particle dynamics and soot kinetics modeling to decrease their costs. To treat soot particle dynamics, discrete sectional methods [12,13] or the method of moments [14–16] have been developed to perform simulations of laminar and turbulent diffusion flames with a reduced number of sections or moments (up to 9 sections or 6 moments).

To describe the formation of soot precursors, various levels of modeling were investigated. Sectional methods gave satisfaction to describe PAH chemistry. Zamuner and Dupoirieux [17] and recently Di Domenico et al. [1] used one along with a PAH-based soot formation model to compute laminar flames [1] and a turbulent one [17], with the aim of applying this approach to gas turbine simulation. However, the PAH formation route remains computationally expensive to describe, except in dedicated codes as the incompressible one of Di Domenico et al. [1].

For that reason, semi-empirical models assume that soot formation is only based on light precursors, such as acetylene, in order to reduce the number of considered species. Many 2D or 3D sooting turbulent flame computations were carried out with the well-known two-equation model of Leung and Lindstedt [18,19], see for example papers [14,20–22], or with the one of Moss and co-workers [23,24], see for example papers [25,26]. Several reduction methods are available to describe acetylene formation in an affordable way. Simplification methods are able to produce comprehensive and accurate simplified reaction mechanisms from detailed ones [27]. However, the species number cannot be sufficiently reduced without losing accuracy on acetylene levels. Another type of reduction method consists in tabulating chemistry and coupling it to the CFD software. It is attractive since it results in a strong decrease of the computational cost. Gicquel et al. [28] proposed the FPI (Flame Prolongation of ILDM) technique, derived from the ILDM (Intrinsic Low-Dimensional Manifolds) method [29]. It indexes the structure of a 1D laminar premixed flame to only one parameter, the progress variable. This method was recently coupled to LES of turbulent premixed combustion [30,31], with the resolved flame structure reconstructed from 1D filtered laminar premixed flames.

Empirical soot models based on global gas-phase kinetics were also developed to obtain a strong decrease of calculation cost. They are based on correlations resulting from experimental measurements. They only depend on mixture fraction [32, 33] or fuel concentration [34,35] and some of them use an intermediate species to model the role of soot precursors i.e. to decorrelate soot formation and fuel oxidation [35,36]. Their low computational cost is attractive but they are inherently not predictive and their conditions of use are limited.

In the context of unsteady simulation of soot formation and radiation in practical combustion devices, the description of detailed chemistry as well as soot and PAH dynamics are not affordable in industrial codes. Semi-empirical soot models coupled with a tabulation method appear to be a good compromise between cost and accuracy of predictions. For these reasons, the strategy proposed in this study involves in a CFD code the FPI tabulation method to describe the gas-phase chemistry, coupled with an improved version of the semi-empirical soot model of Leung et al. [18]. To the author's knowledge, it is the first study about coupling between tabulated gas-phase chemistry and a soot model. This paper describes the first validation step of the strategy, applied to laminar premixed ethylene flames to assess the ability of the strategy to predict soot levels. Radiative transfer was also post-processed in such flames with a Monte Carlo method, in order to emphasize the radiative behavior of soot particles compared to gas-phase species. Coupling between radiation and tabulated chemistry is not treated in this study and will be investigated in future work.

2. Methods and models

2.1. Reacting gas flow

Laminar premixed flames have been simulated with the Onera aerothermochemistry solver, Cedre [37]. This code is based on a cell-centered unstructured finite-volume method that solves the three-dimensional compressible reacting Navier–Stokes equations. This code is able to compute reacting flows in industrial devices with explicit or implicit time-advance numerical schemes and mesh cells with any geometry. Equations of conservation are solved for momentum, mass fractions of chemical species and total energy:

$$\frac{\partial \rho \mathbf{v}}{\partial t} + \nabla \cdot (\rho \mathbf{v} \otimes \mathbf{v}) = \nabla \cdot (\boldsymbol{\tau} - p\mathbf{I}) \tag{1}$$

$$\frac{\partial \rho Y_k}{\partial t} + \nabla \cdot (\rho Y_k \mathbf{v}) = -\nabla \cdot \mathbf{J}_k + \dot{\omega}_k \tag{2}$$

$$\frac{\partial \rho e_t}{\partial t} + \nabla \cdot (\rho e_t \mathbf{v}) = -\nabla \cdot \left(\mathbf{q} + \sum_{k=1}^{n_e} h_k \mathbf{J}_k \right) + \nabla \cdot \left[(\boldsymbol{\tau} - p\mathbf{I})\mathbf{v} \right] + S_{e_t} \tag{3}$$

where ρ is the density, $\mathbf{v}$ the velocity vector, p the pressure, $\boldsymbol{\tau}$ the viscous tensor and $\mathbf{I}$ the identity matrix. The mass fraction, the diffusive flux and the chemical source rate of species k are denoted respectively Y_k, $\mathbf{J}_k$ and $\dot{\omega}_k$. The specific total energy is denoted e_t, the heat flux $\mathbf{q}$, the chemical species number n_e and the specific enthalpy of species k h_k. Moreover, in calculations presented in this study, a source term S_{e_t} is added to the energy equation in order to impose the experimental temperature profile, for reasons explained in Section 3.2. These equations of conservation are closed by a perfect gas state law and relations for transport and thermodynamic properties, including Newton, Fick and Fourier laws for diffusion of momentum, species and heat. Transport of density is not necessary here because it results from summing up all the species balance equations written under conservative form (2).

As the semi-empirical soot model described in Section 2.2 considers acetylene as soot precursor, reacting gas-phase chemistry must contain enough species and reactions to accurately describe acetylene formation. A computationally affordable method consists in tabulating the chemistry as a function of a reduced set of variables. In particular, the FPI method was investigated by Galpin et al. [38] and Savre et al. [39] for combustion in industrial devices. For this method, a one-dimensional laminar premixed flame is pre-processed with the PREMIX code [40] involving complex detailed chemistry and detailed transport. Resulting species mass fractions and source rates are tabulated as functions of a unique and monotonic progress variable c, defined by Eq. (4), which depends on mass fractions of transported species [41]:

$$c = \frac{Y_{CO_2} + Y_{CO}}{Y_{CO_2}^{eq} + Y_{CO}^{eq}} \tag{4}$$

where Y_i^{eq} are constant mass fractions evaluated at the burnt gas outlet boundary of the tabulated flame. The chemical database is coupled to the Navier–Stokes equations solved in Cedre through the transport equations (2) for the main species. Chemical source terms $\dot{\omega}_k$ for these species are extracted from the FPI database knowing the value of the progress variable c, evaluated at each grid cell from transported species CO_2 and CO mass fractions with Eq. (4). It is worth noting that the use of a tabulation method allows to accurately estimate concentrations of only species well correlated with the progress variable. As PAHs and soot have strongly different formation characteristic time scales than those of chemical species on which the progress variable is based, they are decorrelated from these species. Then they cannot be tabulated along with the same progress variable. Consequently, an acetylene-based soot model was preferred to PAH-based soot models or soot tabulation. Actual correlation between acetylene and the progress variable defined by Eq. (4) will be verified in Section 4.1.

2.2. Soot model

The soot model is derived from the semi-empirical model of Leung et al. [18]. It was largely used and adapted to different flames and fuels (see for example papers [20,22,42–44]). It includes integration of two additional transport equations for the soot mass fraction Y_s and the particle number per mass unit of mixing N. These equations can be written for an unsteady flow as

$$\frac{\partial \rho Y_s}{\partial t} + \nabla \cdot (\rho Y_s \mathbf{v}) = -\nabla \cdot \mathbf{J}_s + \dot{\omega}_s \tag{5}$$

$$\frac{\partial \rho N}{\partial t} + \nabla \cdot (\rho N \mathbf{v}) = -\nabla \cdot \mathbf{J}_N + \dot{\omega}_N \tag{6}$$

where $\mathbf{J}_s = -\mu \nabla Y_s$ and $\mathbf{J}_N = -\mu \nabla N$ are diffusive fluxes, with μ the mixture dynamic viscosity. Differential diffusion of soot and thermophoresis transport were not considered in this study.

Nucleation, surface growth, oxidation and agglomeration steps of soot formation are taken into account as source terms in Eqs. (5) and (6). The transport equation for N is only necessary to evaluate the total soot surface area needed for growth and oxidation steps of the model. The model is closed by simplifying assumptions of a spherical particle shape and a monodisperse size distribution. Moreover soot is considered to be entirely carbon with a density ρ_s of 2000 $\mathrm{kg\,m^{-3}}$. With these assumptions, an equivalent particle diameter can be defined from Y_s and N as

$$d_p = \left(\frac{6 Y_s}{\pi \rho_s N} \right)^{1/3} \tag{7}$$

The total soot surface area S ($\mathrm{m^2\,m^{-3}_{mixture}}$) can be formulated as

$$S = \pi d_p^2 \rho N \tag{8}$$

This original simple model was improved according to Lindstedt's findings [19] and adapted to premixed combustion, as described below. Sections 2.2.1 to 2.2.4 describe each model step with their contribution to source terms of soot mass fraction and particle number, involving Arrhenius rate constants $\mathcal{K}_r(T)$. Reaction rates $\dot{W}_r$ are expressed in $\mathrm{mol\,m^{-3}\,s^{-1}}$ units.

2.2.1. Nucleation

This step models incipient soot particle formation. It gives rise to an increase of soot mass fraction and particle number. Acetylene is assumed to be the only incipient species for soot nucleation. Chemical reaction is written

$$C_2H_2 \rightarrow 2C_s + H_2 \tag{9}$$

The reaction rate is formulated with the assumption of a first-order dependence on acetylene concentration, as Eq. (10), where index n denotes the nucleation step:

$$\dot{W}_n = \mathcal{K}_n(T)[C_2H_2] \tag{10}$$

Lindstedt [19] suggested that nucleation step represents both formation of incipient soot particles and initial soot mass growth. In this way, created particles are assumed to contain a minimum number of carbon atoms $C_{\min}$, chosen as Leung et al. [18] equal to 100. Nucleation part of the particle number source term (in particles $\mathrm{m}^{-3}\,\mathrm{s}^{-1}$) may be written as Eq. (11) [18,19], where $\mathcal{N}_A$ is Avogadro's number.

$$\dot{\omega}_{N,n} = \frac{2}{C_{\min}}\mathcal{N}_A\dot{W}_n \tag{11}$$

2.2.2. Surface growth

The main part of the mass growth is obtained by chemical reaction taking place at the surface of the particles. This mechanism is known as surface growth. According to the well-known surface-HACA (H-Abstraction-C_2H_2-Addition) mechanism proposed by Frenklach and Wang [45] and experimental observations of Harris and Weiner [46], surface growth is assumed to be dominated by acetylene addition on soot surface. The corresponding chemical reduced equation is similar to Eq. (9) for nucleation [18]:

$$C_2H_2 + C_s \rightarrow 3C_s + H_2 \tag{12}$$

Its reaction rate is written:

$$\dot{W}_g = \mathcal{K}_g(T)f(S)[C_2H_2] \tag{13}$$

where index g denotes the surface growth step. A function of the available total soot surface $f(S)$ was originally introduced to take effects of surface chemistry into account. The early proposed function $f(S) = S^{1/2}$ [18] gave good results, in agreement with other studies [43,47–49]. However, for a given particle size, the soot surface growth is proportional to the soot particle number if interactions between particles are negligible. This implies that $f(S)$ must be proportional to the total soot surface area S and not to the square root of S. Xu et al. [50] have observed the decrease of the surface growth rate with the increase of residence time in premixed laminar ethylene/air flames. They suggested that this decrease may be due to the lack of hydrogen atoms in the downstream colder zone of the flame, which prevents active sites from being created according to the HACA mechanism. As the surface of primary particles strictly increases toward downstream in rich premixed flames, a simple way to model the decrease of the active site number in such flames is to use the function $f(S) = S_1^{\alpha}\rho N$, where $S_1 = \pi d_p^2$ is the surface of one soot particle and α is an arbitrary coefficient. Several values from 0 to 1 for α were investigated and corresponding results will be presented in Section 4.2.2.

2.2.3. Oxidation

According to Kronenburg et al. [22], Yunardi et al. [20] and comments of Leung et al. [18], oxidation by OH was added to the original oxidation step by O_2, in order to describe with more accuracy soot oxidation in premixed flames. Chemical reactions of O_2 and OH oxidation steps are written as:

$$C_s + \tfrac{1}{2}O_2 \rightarrow CO \tag{14}$$

$$C_s + OH \rightarrow CO + H \tag{15}$$

Corresponding reaction rates are formulated:

$$\dot{W}_{ox}^{O_2} = \mathcal{K}_{ox}^{O_2}(T)S[O_2] \tag{16}$$

$$\dot{W}_{ox}^{OH} = \mathcal{K}_{ox}^{OH}(T)S[OH] \tag{17}$$

However, in 1D laminar premixed flame cases described in Section 3, soot oxidation by OH was observed to have no effect on soot predictions. Therefore it has been neglected in order to avoid the calculation of the concentration of H and OH species.

2.2.4. Agglomeration

Leung et al. [18] suggested modeling soot particle agglomeration by the simple reaction (18) which induces a source term for the particle number transport equation:

$$n\mathrm{C_s} \rightarrow (\mathrm{C_s})_n \tag{18}$$

This considers that particles agglomerate into bigger particles of spherical shape, far from the real fractal-like shape of the agglomerates observed in diffusion and partially premixed flames (see, for example, Arana et al. [51]). These agglomerates are actually made up of chains of identifiable primary particles. As argued by Ezekoye and Zhang [52] and Liu et al. [48], it appears more appropriate to estimate the total soot surface area from unagglomerated primary particles than from big spherical agglomerates. That is why the original agglomeration step (18) is not considered here. Finally, it amounts to neglect the finite area contact joints between primary particles inside non-spherical agglomerates. The number N of soot particles per mass unit of mixing hence becomes the number of primary soot particles per mass unit of mixing, regardless of whether or not they be agglomerated.

Moreover, the soot particles produced in flames similar to the ones simulated in this Note were analyzed by Abid et al. [53] and Öktem et al. [54] using TEM (Transmission Electron Microscopy). Almost only nearly spherical particles were observed, meaning that agglomeration process did not occur in the investigated flames.

2.2.5. Synthesis

Finally, considering all the modeling of Sections 2.2.1 to 2.2.4, soot mass fraction and particle number source terms, respectively in $\mathrm{kg\,m^{-3}\,s^{-1}}$ and in $\mathrm{particles\,m^{-3}\,s^{-1}}$, are written:

$$\dot{\omega}_s = \underbrace{2\mathcal{M}_{\mathrm{C_s}}\dot{W}_n}_{\dot{\omega}_{s,n}} + \underbrace{2\mathcal{M}_{\mathrm{C_s}}\dot{W}_g}_{\dot{\omega}_{s,g}} - \underbrace{\mathcal{M}_{\mathrm{C_s}}\dot{W}_{\mathrm{ox}}^{\mathrm{O_2}}}_{\dot{\omega}_{s,\mathrm{ox}\mathrm{O_2}}} - \underbrace{\mathcal{M}_{\mathrm{C_s}}\dot{W}_{\mathrm{ox}}^{\mathrm{OH}}}_{\dot{\omega}_{s,\mathrm{ox}\mathrm{OH}}} \tag{19}$$

$$\dot{\omega}_N = \dot{\omega}_{N,n} \tag{20}$$

with $\mathcal{M}_{\mathrm{C_s}}$ the molar mass of soot carbon, and $\dot{\omega}_{s,k}$ the contribution of the soot formation step k to the soot mass source rate $\dot{\omega}_s$.

2.3. Radiative transfer

Radiative transfer computations were performed with a Monte Carlo method. Its principle is to replace multiple integrals by finite sums on a large number of stochastically-generated optical paths. Forward and reciprocal formulations detailed in the paper of Tessé et al. [55] were tested on the premixed flames described in Section 3.

Concerning the gas phase, only H_2O and CO_2 were taken into account. Their radiative properties were treated in a correlated manner by the CK model used by Tessé et al. [55,56]. Effects of scattering by soot particles have been shown negligible by Eymet et al. [57]. Therefore, only emission and absorption have to be taken into account, and the spectral soot absorption coefficient can be deduced from the soot volume fraction f_v by the relation $\kappa_{\nu,s} = 550\nu f_v$, where ν is the wavenumber (in $\mathrm{cm^{-1}}$).

3. Simulated test cases

3.1. Experimental conditions

Two laminar premixed ethylene flames were simulated in this study. The first is a fuel-rich ethylene–air flame experimentally investigated by Xu et al. [50]. This flame was studied numerically by Appel et al. [8] and more recently by Mehta et al. [58]. A water-cooled porous-plate burner was used to stabilize a laminar premixed flat-flame at atmospheric pressure. A coflow of nitrogen surrounded the fuel-rich ethylene–air mixture to prevent it from burning with ambient air. A flat plate with a hole was placed above the flame to ensure its stabilization. Temperature, concentrations of major gas species, soot volume fraction and soot primary particle diameter were measured for three different fuel equivalence ratios. These three sets of conditions are designated as flames XSF2.33, XSF2.64 and XSF2.93 in this paper, according to a nomenclature constructed from the initials of the corresponding authors followed by the fuel-equivalence ratio. More details on experimental conditions and measurement methods are given by Xu et al. [50].

The second flame ZYW2.07 is a laminar premixed ethylene–oxygen–argon flame at equivalence ratio $\phi = 2.07$, studied experimentally by Zhao et al. [59] and numerically in a companion paper [60] and also by Mehta et al. [58]. A water-cooled porous plug burner was used, with an argon coflow shroud. Temperature, PSDF (Particle Size Distribution Function) and soot volume fraction were reported by experimental measurements. Table 1 gives inlet conditions for the four different flame cases.

Table 1
Summary of flame conditions.

	Flame designation/reference			
	XSF2.33/[50]	XSF2.64/[50]	XSF2.93/[50]	ZYW2.07/[59]
[C]/[O]	0.78	0.88	0.98	0.69
Fuel-equivalence ratio ϕ	2.33	2.64	2.93	2.07
Dilution ratio	3.31	3.30	3.30	4.37
Reactant mixture	$C_2H_4/O_2/N_2$	$C_2H_4/O_2/N_2$	$C_2H_4/O_2/N_2$	$C_2H_4/O_2/Ar$
Reactant flow rate ($kg\,m^{-2}\,s^{-1}$)	7.961×10^{-2}	7.958×10^{-2}	6.168×10^{-2}	1.266×10^{-1}

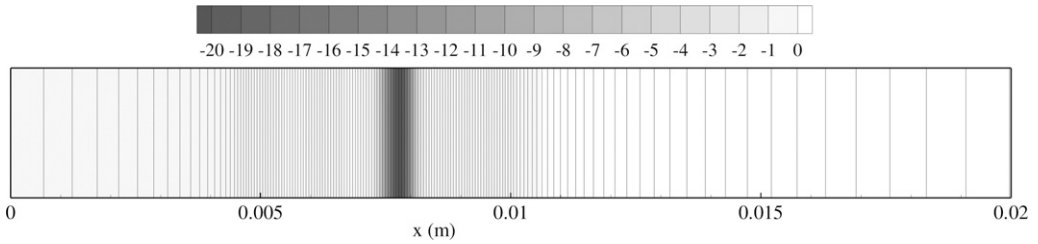

Fig. 1. Detail of the mesh used for the 1D flame calculations, colored by the ethylene reaction rate ($kg\,m^{-3}\,s^{-1}$).

3.2. Numerical conditions

3.2.1. Table construction

For each flame case in Table 1, the experimental flame was simulated in one dimension, without modeling nitrogen or argon coflows. Such a coflow has a shielding effect on the flame, which prevents from reaction with ambient air. But the coflow also generates heat exchanges which may affect the flame temperature. Therefore in our 1D calculations, the experimental temperature profile was imposed on the whole domain to take into account this coflow thermal effect as well as thermal effects of the stabilization flat plate and radiation. In a first step, to generate the FPI table, the stationary flame was computed without soot model with the PREMIX code [40], with the experimental mixture flow rate prescribed as inlet boundary condition. The detailed chemical mechanism of Qin et al. [61] involving 70 species up to C_6H_6 and 463 reactions was used to describe ethylene chemistry.

3.2.2. CFD calculation

In a second step, the generated FPI table was used with the coupling technique described in Section 2.1 to compute the unsteady one-dimensional flame with Cedre involving the previously described soot model to evaluate soot volume fraction levels. In rich ethylene flames, most important species in terms of mass and energy are C_2H_4, O_2, H_2O, CO_2, CO, C_2H_2, C_4H_2, H_2 and N_2 (or Ar, see Table 1). These nine species were transported, in addition with soot C_s needed by soot modeling.

Because of their small size, soot particles move with the gaseous flow. Moreover, the soot volume fraction is usually very low in flames (mostly less than 10^{-5}). For these reasons, soot is treated in the same way as other gaseous species, i.e. with the same state and mixing laws.

Soot particles also interact with other gas-phase species through production and consumption terms added to chemical sources extracted from the FPI table. Consequently a two-way coupling between soot precursors and soot particles is taken into account although the tabulated chemistry is not directly influenced by the soot model. For energy considerations, soot thermodynamic properties are assumed to be those of solid carbon.

Numerical domain was 41 mm long and non-uniformly discretized in 163 cells, with about 20 cells in the flame front. Fig. 1 shows the refined zone which contains the flame front. The inlet boundary conditions are given in Table 1. A characteristic non-reflecting condition [62] was fixed on the outlet boundary in order to evacuate pressure waves occurring at first iterations. The initial chemical state was given by flame calculation achieved with the PREMIX code. The energy balance was corrected to impose the experimental temperature profile in Cedre, for the same reasons as in PREMIX. Flame propagation was computed during 160 ms from initial state. This duration was necessary to obtain stabilized soot levels on the whole computed domain. It was possible to use a one-step Euler implicit method for time marching because acoustics do not affect final results. Used with a time step based on chemical species time scales (about 3×10^{-6} s), it led to a speed-up factor of 20 to 30 on CPU time compared to a second-order explicit Runge–Kutta method with time step limited by the CFL condition (about 3×10^{-8} s). It is worth noting that results obtained with the implicit method have been successfully validated against those obtained with the explicit method. The Cedre calculation took 40 min on a single 2.8 GHz core of a quad-core Intel Nehalem processor.

3.2.3. Radiative transfer

Radiative transfer was computed in a post-processing step because imposed temperature profile in flame calculation already takes radiation effects into account along with other heat losses. The aim of such a calculation is to evaluate sepa-

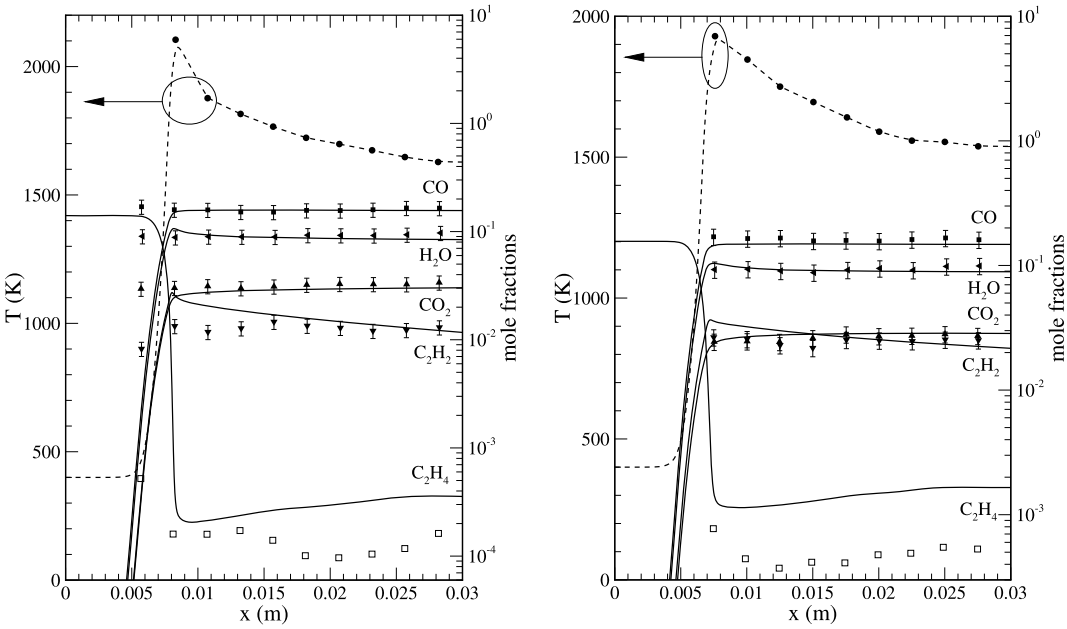

(a) flame XSF2.33 ($\phi = 2.33$). (b) flame XSF2.64 ($\phi = 2.64$).

Fig. 2. Temperature and main species mole fractions in flames XSF2.33 and XSF2.64. Experimental measurements (symbols) and model predictions (lines).

rate roles of gas-phase species and soot particles in radiative transfer and to qualify their respective influence at different wavelengths. A 3D mesh was extruded from the one used for aerothermochemistry calculation, but without discretizing transverse dimensions of the 1D test case. The canal section is equal to the burner exit area, to simulate radiation in the estimated whole flame volume. Lateral faces and flow inlet and outlet faces were considered as non-emitting radiative outlets. Incoming radiation emitted by the outside was neglected, except downstream for calculations shown in Fig. 10.

4. Results and discussion

4.1. Gas phase chemistry

Mole fractions of major gas-phase species have been compared to experimental measurements reported in the paper of Xu et al. [50]. Temperature and mole fraction profiles were plotted for flames XSF2.33, XSF2.64 and XSF2.93 in Figs. 2a, 2b and 3a respectively.

For these flames, the temperature profile has to be estimated in the soot-free region near the burner surface, because of the lack of measurement. Compared to previous numerical studies [8,50,58], assumption of a stiff temperature profile was preferred to linearly interpolation between the assumed burner surface temperature and the first measurement point located in the flame front. That is the reason why measured mole fractions at upstream measurement points ($x \leqslant 0.008$ m) are not numerically correctly reproduced (see e.g. Fig. 2a). Computed mole fraction profiles appeared to be slightly translated downstream compared to similar profiles obtained by Appel et al. [8] in the flame XSF2.64 with a linearly interpolated temperature profile upstream the first measurement point. The real temperature profile probably lies between a linear profile and the stiff profile used here.

Except for ethylene, numerical predictions show a good agreement with the experiment for flames XSF2.33, XSF2.64 and XSF2.93. Plotted error bars are maximal uncertainties estimated by Xu et al. to be 15 % for mole fractions greater than 5×10^{-3}. For ethylene mole fraction, significant discrepancies are observed but uncertainties are known to be greater than 15 % [50]. Appel et al. [8] also observed discrepancies for ethylene mole fractions on the same flame with a more detailed chemical scheme based on the 99-species mechanism of Wang and Frenklach [7].

In Fig. 3b, mole fraction of the soot precursor species, acetylene, is plotted along the height above the burner for flame XSF2.93. The 1D code PREMIX involving the detailed chemical scheme of Qin et al. [61] and the CFD code Cedre involving the tabulation method give very similar results when soot is not taken into account. When the soot model is added, acetylene mole fractions obtained in our calculation become closer to those given by the experiment and are found in the range of experimental uncertainties. This effect of coupling between gas-phase and soot chemistry will also contribute to improve soot predictions. However, the accuracy of C_2H_2 predictions decreases near the flame front with decreasing fuel equivalence ratio, whereas it remains satisfactory downstream (see Fig. 2). Several reasons are suspected, including temperature profile assumption upstream the first measurement point, and the kinetic scheme used, since Appel et al. [8] obtained more precise C_2H_2 predictions at $\phi = 2.64$. The tabulation method coupled with the soot model is nevertheless able to

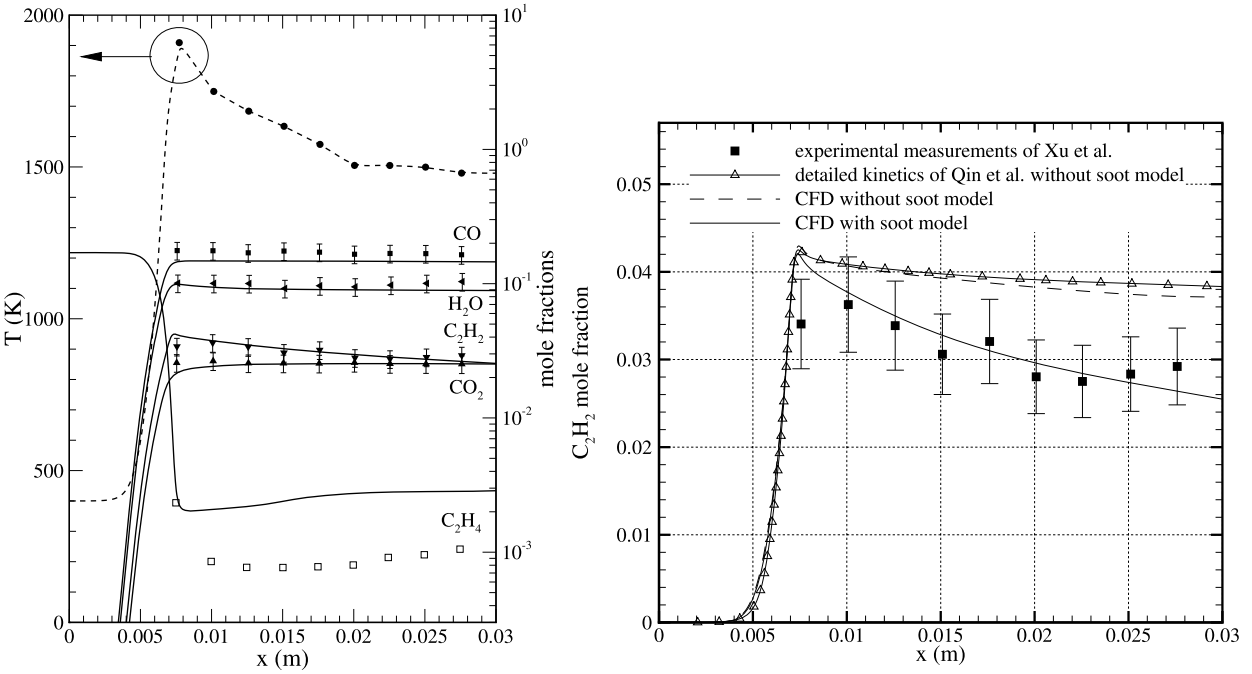

(a) Experimental measurements (symbols) and model predictions (lines).

(b) C_2H_2 mole fraction profiles obtained for flame XSF2.93.

Fig. 3. Temperature and main species mole fractions in flame XSF2.93 ($\phi = 2.93$).

reproduce acetylene levels in such rich flame. Being based on acetylene and coupled to the gas-phase chemistry, the semi-empirical soot model is physically limited by its acetylene consumption. It is not the case of empirical soot models, e.g. the Tesner–Magnussen model [35,63], which have to introduce empirical limitations instead.

4.2. Soot results

4.2.1. Model parameter optimization

The soot model described in Section 2.2 has been used to simulate laminar premixed flames, while Leung and Lindstedt [18,19] developed it for laminar counterflow flames. As emphasized by Lautenberger et al. [33], soot formation is not controlled by the same parameters in premixed combustion as in diffusion flames. In premixed combustion, heterogeneous reactions (nucleation, surface growth and oxidation) are rate-limiting steps and the soot surface area is the most important parameter controlling them, whereas in diffusion flames, soot formation is mainly controlled by gas-phase reactions outside the flame front.

Because of these differences and due to the empirical nature of the soot model, its constants were optimized for ethylene premixed combustion. Soot model parameters were modified to fit soot volume fraction and particle number to experimental results of flame XSF2.64. For the soot surface growth sub-model, soot surface area function was assumed to be $f(S) = \rho N$, i.e. $\alpha = 0$ in the expression of $f(S)$ introduced in Section 2.2.2. The low influence of α on the soot volume fraction will be shown in Section 4.2.2. As described in Fig. 7 and in the paper of Mehta et al. [58], surface growth was found to be the dominant step for soot mass change, whereas nucleation step controls the increase of particle number. Therefore, optimization of model parameters consisted in adjusting surface growth pre-exponential factor to the measured soot volume fractions, and nucleation pre-exponential factor to the primary particle number per volume unit of mixing $n_p = \rho N$ calculated by Xu et al. [50] from measured primary soot particle diameter. In this study, the particle number per mass unit of mixing N given by the model can be directly compared to n_p because agglomeration is not considered in the soot model.

Resulting constants are summarized in Table 2, where A, β and T_a are respectively pre-exponential factor, temperature exponent and activation energy of Arrhenius rate constants defined as in Eq. (21):

$$\mathcal{K}(T) = AT^{\beta} \exp\left(-\frac{T_a}{T}\right) \tag{21}$$

Only pre-exponential factors for nucleation and surface growth were modified from the original model. To compute flames XSF2.33, XSF2.93 and ZYW2.07, the same soot model parameters as for XSF2.64 flame were used.

Table 2
Summary of model constants. Units are mol, m, s, K.

	A	β	T_a	References
Nucleation	7.7×10^4	0	21 100	A: adjusted, β and T_a: [18]
Surface growth	3.0×10^{-10}	0	12 100	A: adjusted, β and T_a: [18]
O_2 oxidation	7.15×10^6	0.5	19 800	[18,68]
OH oxidation	3.6×10^2	0.5	0	[22,69]

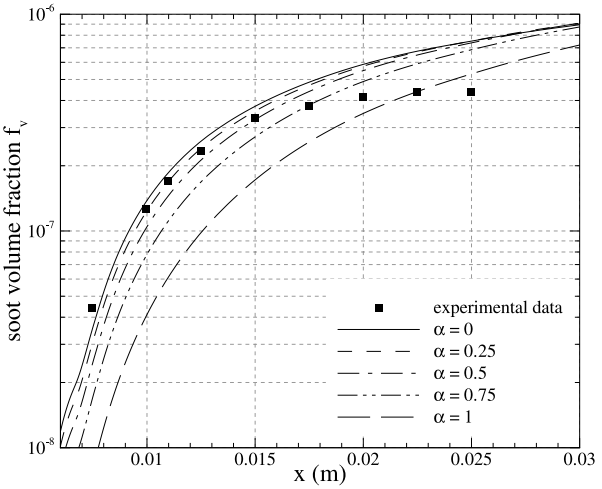

Fig. 4. Soot volume fractions obtained in flame XSF2.64 for different types of soot surface area functions.

4.2.2. Soot surface growth modeling

Dealing with the soot surface area function $f(S) = S_1^{\alpha} \rho N$, several values from 0 to 1 for α were investigated on the computed flame XSF2.64. Obtained soot volume fraction profiles are compared with the experimental profile in Fig. 4. Model parameters used in these calculations are those obtained after optimization for $\alpha = 0$ i.e. $f(S) = \rho N$ (see Table 2). However, the surface growth pre-exponential factor A_g was adjusted depending on the value of α because it induces a change of the unit of $f(S)$. The low influence of the parameter α on the shape of the soot volume fraction profile is demonstrated in Fig. 4.

Results presented in the next sections were obtained with the retained function $f(S) = \rho N$ ($\alpha = 0$), which means that big soot particles have a lower surface reactivity than small particles, for a fixed mass of soot. This result is in agreement with findings of Lindstedt [19].

4.2.3. Soot volume fraction results

Soot volume fraction profiles, deduced from soot mass fraction Y_s through the relation $f_v = Y_s \rho / \rho_s$, are presented in Fig. 5 for the four flames investigated and compared to experimental data. These data were obtained with an optical method (laser extinction) by Xu et al. [50] for $\phi = 2.33$, $\phi = 2.64$ and $\phi = 2.93$, whereas for $\phi = 2.07$, Zhao et al. [59] used in situ probe sampling with online analysis using a nano scanning mobility particle sizer. Numerical results were obtained with an imposed experimental temperature profile measured with a non-intrusive technique. Therefore they cannot be directly compared to probe sampling measurements. To account for the probe disturbances on the flow field and on temperature and concentration profiles, experimental measurements of Zhao et al. [59] have been shifted by 3 mm upstream toward the burner, as supported in previous investigations [58,60,64–66]. Profile-shifting has been recognized as a standard method to compare profiles measured with intrusive and non-intrusive techniques although it has no theoretical basis [67].

Soot volume fractions increase with the flame height, downstream the flame front located around 8 mm above the burner. For flames of Xu et al. [50], f_v is predicted within a factor of 3 from experimental data. Appel et al. [8] found the same discrepancies between experimental data and predictions of their detailed soot model, when using the same set of parameters to compute all flames. The larger discrepancies concerning f_v observed at $\phi = 2.33$ can be explained by the quality of the C_2H_2 prediction which has been discussed in Section 4.1. At $\phi = 2.07$, the model is compared with an intrusive technique of measurement. It overestimates soot volume fraction up to 1.2 cm above the burner and underestimates it downstream by a maximum factor of 7. However, it is worth noting that experimental measurements at $\phi = 2.07$ cross those at $\phi = 2.33$ around $x = 1.5 \times 10^{-2}$ m, whereas the ZYW2.07 flame is cooler ($\sim$ 1600 K) than the XSF2.33 flame ($\sim$ 1750 K) and its equivalence ratio (2.07) is lower than other investigated flames. Consequently, experimental soot volume fraction at $\phi = 2.07$ are expected to be lower than at $\phi = 2.33$.

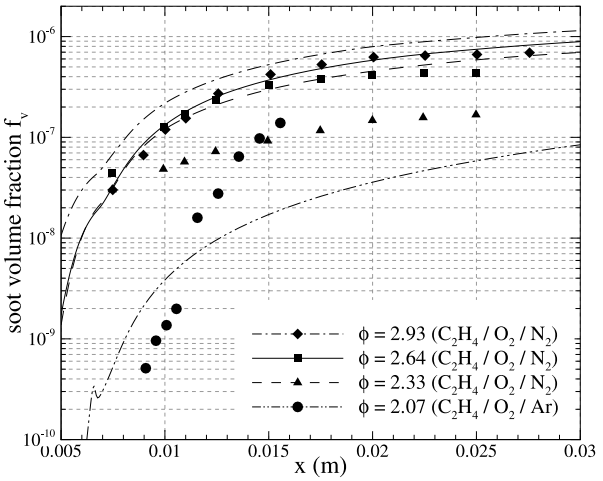

Fig. 5. Soot volume fraction profiles along the flame axis in flames XSF2.33, XSF2.64, XSF2.93 and ZYW2.07. Experimental measurements [50,59] (symbols) and model predictions (lines).

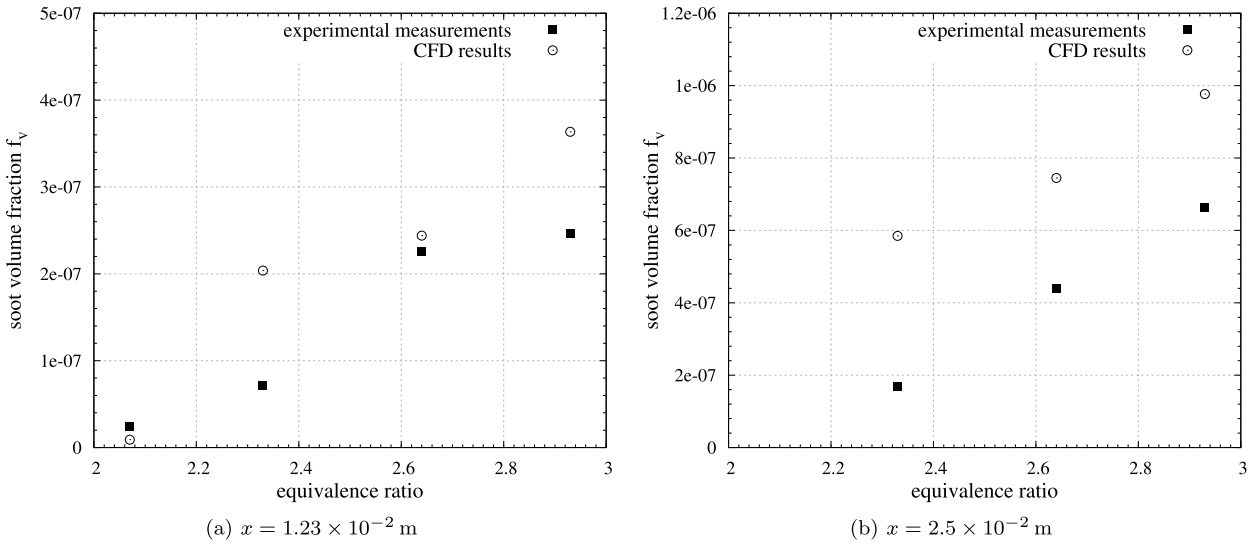

Fig. 6. Experimental and computed soot volume fractions according to the equivalence ratio at two axial locations.

At two representative heights above the burner, experimental and numerical soot volume fractions were plotted against the equivalence ratio in Fig. 6. As expected, soot volume fraction rises when equivalence ratio increases, due to increasing acetylene concentration with the equivalence ratio. Compared to experimental data, the general trend is correctly reproduced, whereas discrepancies are acceptable. Mehta et al. [58] found similar differences in the same flames with more detailed modeling of soot formation.

To have a deeper insight on the model behavior, contributions of the soot model steps to the soot mass source rate, defined in Eq. (19) as $\dot{\omega}_{s,n}$, $\dot{\omega}_{s,g}$ and $\dot{\omega}_{s,\mathrm{ox}O_2}$, are plotted in Fig. 7 for flame XSF2.93. The nucleation rate is by three orders lower than surface growth and oxidation rates. It mainly contributes to the production of soot particles just after the flame front, and decreases downstream with the temperature and acetylene concentration. Surface growth is the dominant step of the model, approximately fifteen times higher than O_2 oxidation as expected in such a fuel-rich flame. Surface growth rate increases with soot surface area and decreases downstream with temperature and acetylene concentration. Correlated with the O_2 concentration, oxidation is only significant near the flame front.

4.3. Flame radiation

Radiative transfer was computed in a post-processing step from results reported above. Flame XSF2.64 was chosen to detail spatial and spectral distributions of the radiative power in such a rich premixed flame. The conventional Forward Method (FM) converges more rapidly than other methods in this configuration, as observed by Tessé et al. in an optically

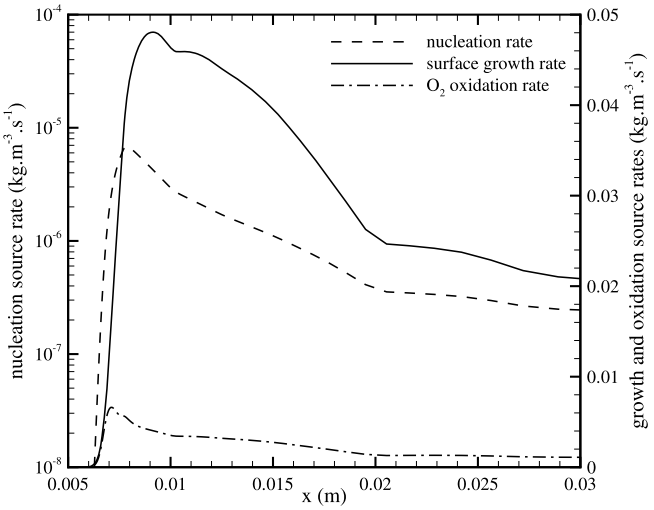

Fig. 7. Soot formation step source rates obtained in the laminar premixed ethylene–air flame XSF2.93 ($\mathrm{kg\,m^{-3}\,s^{-1}}$).

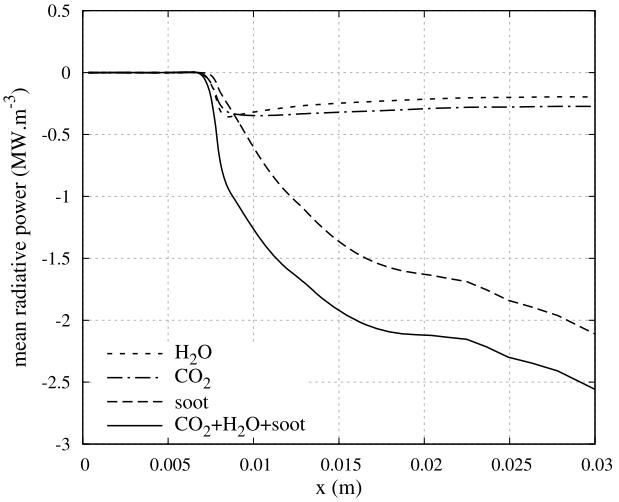

Fig. 8. Gas and soot contributions to the radiative power in flame XSF2.64.

thin medium of gas mixture (case 6 of [55]). In Fig. 8 total radiative powers are plotted for H_2O, CO_2 and soot considered separately, and for the mixture of these components. Spectral radiative powers at $x = 0.03$ m are plotted in Fig. 9. Radiative energy loss of the flame appears to be mainly due to soot particles (about 80 % of total radiative power).

The main uncertainty of radiative transfer modeling with the 1D approximation in this flame lies in estimating roles of the stabilization plate and the hot burnt gases downstream the flame. To evaluate the influence of the downstream radiative boundary condition, incoming radiation from the outside was taken into account with an emitting black wall at various temperatures. Total radiative powers are compared in Fig. 10 to the previous one obtained with a non-emitting radiative outlet, for the $H_2O + CO_2 +$ soot mixture. Outside emission can reduce the absolute value of radiative power loss of less than 10 %. It is worth noting that 1D approximation is valuable for combustion and soot formation calculation but not for radiative transfer modeling which depends on the 3D experimental conditions.

5. Conclusion

Laminar premixed 1D ethylene-rich flames were computed with a CFD compressible code, involving a tabulation FPI method for detailed gas-phase chemistry and a semi-empirical soot model. In addition, radiative transfer was post-processed with a Monte Carlo method for gas and soot radiation. Major chemical species were well described by the FPI tabulation method, compared to measurements. In particular, prediction of soot precursor species such as acetylene was improved when the soot formation is modeled. The surface growth dependence on total soot surface area was investigated. A dependence on the particle number instead of on the soot surface area was found to give soot volume fractions closer to experimental data. The soot model parameters were adjusted for one equivalence ratio, and applied without further modifi-

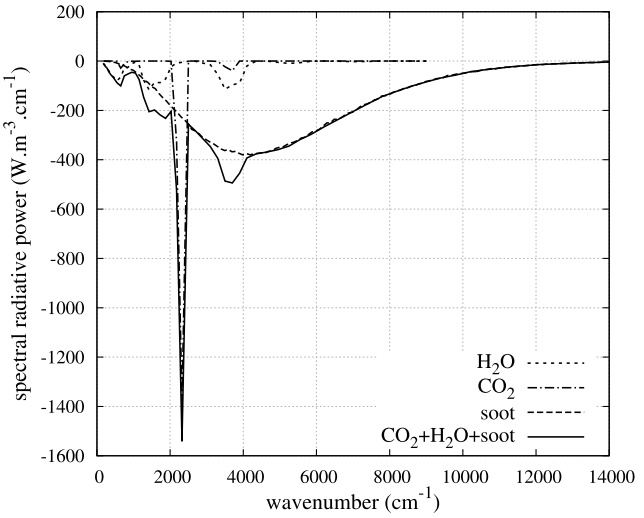

Fig. 9. Gas and soot contributions to the spectral radiative power at $x = 0.03$ m in flame XSF2.64.

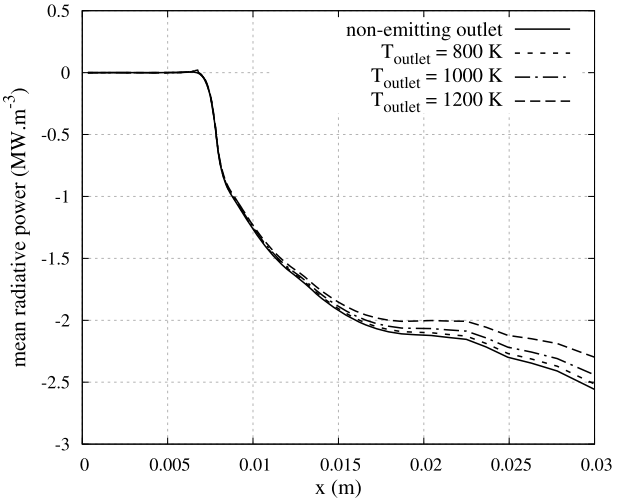

Fig. 10. Total radiative powers in flame XSF2.64 obtained with different downstream radiative boundary conditions.

cations to other equivalence ratios. The evolution of soot volume fraction with the equivalence ratio is similar to predictions of more detailed models involved in other studies [8,58]. Finally, the innovative methodology based on the FPI tabulation method coupled with a semi-empirical soot model was successful to predict soot precursors and soot particles levels in rich premixed laminar flames. Moreover, soot particles were shown to dominate radiative transfer in such a sooting flame, compared to H_2O and CO_2 species. Therefore soot radiation cannot be neglected to correctly evaluate heat transfer.

After this first validation step, the modeling strategy will be applied to a combustion chamber to model unsteady turbulent combustion with soot formation and coupled radiative transfer. For this, the FPI tabulation method will be extended to partially premixed combustion and radiative flames in adding respectively the mixture fraction and the enthalpy as additional dimensions to the FPI database (as in the paper of Fiorina et al. [41]). Moreover full coupling between aerothermochemistry and radiative transfer phenomena will be taken into account. Modeling of interactions between turbulence and gas-phase chemistry, soot and radiation is known as a crucial key point [2] that will be addressed in a future study.

References

[1] M. Di Domenico, P. Gerlinger, M. Aigner, Development and validation of a new soot formation model for gas turbine combustor simulations, Combust. Flame 157 (2010) 246–258.

[2] R.S. Mehta, D.C. Haworth, M.F. Modest, Composition PDF/photon Monte Carlo modeling of moderately sooting turbulent jet flames, Combust. Flame 157 (2010) 982–994.

[3] G. Boudier, L.Y.M. Gicquel, T. Poinsot, D. Bissières, C. Bérat, Comparison of LES, RANS and experiments in an aeronautical gas turbine combustion chamber, Proc. Combust. Inst. 31 (2007) 3075–3082.

[4] G. Boudier, L.Y.M. Gicquel, T.J. Poinsot, Effects of mesh resolution on large eddy simulation of reacting flows in complex geometry combustors, Combust. Flame 155 (2008) 196–214.
[5] P. Schmitt, T. Poinsot, B. Schuermans, K.P. Geigle, Large-eddy simulation and experimental study of heat transfer, nitric oxide emissions and combustion instability in a swirled turbulent high-pressure burner, J. Fluid Mech. 570 (2007) 17–46.
[6] H. Wang, Formation of nascent soot and other condensed-phase materials in flames, Proc. Combust. Inst. 33 (2011) 41–67.
[7] H. Wang, M. Frenklach, A detailed kinetic modeling study of aromatics formation in laminar premixed acetylene and ethylene flames, Combust. Flame 110 (1997) 173–221.
[8] J. Appel, H. Bockhorn, M. Frenklach, Kinetic modeling of soot formation with detailed chemistry and physics: laminar premixed flames of C_2 hydrocarbons, Combust. Flame 121 (2000) 122–136.
[9] A. D'Anna, J.H. Kent, R.J. Santoro, Investigation of species concentration and soot formation in a co-flowing diffusion flame of ethylene, Combust. Sci. Technol. 179 (2007) 355–369.
[10] R.J. Santoro, T.T. Yeh, J.J. Horvath, H.G. Semerjian, The transport and growth of soot particles in laminar diffusion flames, Combust. Sci. Technol. 53 (1987) 89–115.
[11] Q. Zhang, M.J. Thomson, H. Guo, F. Liu, G.J. Smallwood, A numerical study of soot aggregate formation in a laminar coflow diffusion flame, Combust. Flame 156 (2009) 697–705.
[12] M.B. Colket, R.J. Hall, Successes and uncertainties in modeling soot formation in laminar, premixed flames, in: H. Bockhorn (Ed.), Soot Formation in Combustion: Mechanisms and Models, Springer-Verlag, New York, 1994, pp. 442–470.
[13] C.S. McEnally, A.M. Schaffer, M.B. Long, L.D. Pfefferle, M.D. Smooke, M.B. Colket, R.J. Hall, Computational and experimental study of soot formation in a coflow, laminar ethylene diffusion flame, Symp. (Int.) Combust. 27 (1998) 1497–1505.
[14] R.P. Lindstedt, S.A. Louloudi, Joint-scalar transported PDF modeling of soot formation and oxidation, Proc. Combust. Inst. 30 (2005) 775–783.
[15] F. Mauss, K. Netzell, H. Lehtiniemi, Aspects of modeling soot formation in turbulent diffusion flames, Combust. Sci. Technol. 178 (2006) 1871–1885.
[16] H. Guo, G.J. Smallwood, A numerical study on the influence of CO_2 addition on soot formation in an ethylene/air diffusion flame, Combust. Sci. Technol. 180 (2008) 1695–1708.
[17] B. Zamuner, F. Dupoirieux, Numerical simulation of soot formation in a turbulent flame with a Monte Carlo PDF approach and detailed chemistry, Combust. Sci. Technol. 158 (2000) 407–438.
[18] K.M. Leung, R.P. Lindstedt, W.P. Jones, A simplified reaction mechanism for soot formation in nonpremixed flames, Combust. Flame 87 (1991) 289–305.
[19] P.R. Lindstedt, Simplified soot nucleation and surface growth steps for non-premixed flames, in: H. Bockhorn (Ed.), Soot Formation in Combustion: Mechanisms and Models, Springer-Verlag, New York, 1994, pp. 417–441.
[20] Yunardi, R.M. Woolley, M. Fairweather, Conditional moment closure prediction of soot formation in turbulent, nonpremixed ethylene flames, Combust. Flame 152 (2008) 360–376.
[21] D.O. Lignell, J.C. Hewson, J.H. Chen, A-priori analysis of conditional moment closure modeling of a temporal ethylene jet flame with soot formation using direct numerical simulation, Proc. Combust. Inst. 32 (2009) 1491–1498.
[22] A. Kronenburg, R.W. Bilger, J.H. Kent, Modeling soot formation in turbulent methane–air jet diffusion flames, Combust. Flame 121 (2000) 24–40.
[23] J.B. Moss, C.D. Stewart, K.J. Young, Modeling soot formation and burnout in a high temperature laminar diffusion flame burning under oxygen-enriched conditions, Combust. Flame 101 (1995) 491–500.
[24] K.J. Syed, C.D. Stewart, J.B. Moss, Modelling soot formation and thermal radiation in buoyant turbulent diffusion flames, Proc. Combust. Inst. 23 (1991) 1533–1541.
[25] S.J. Brookes, J.B. Moss, Predictions of soot and thermal radiation properties in confined turbulent jet diffusion flames, Combust. Flame 116 (1999) 486–503.
[26] O.V. Roditcheva, X.S. Bai, Pressure effect on soot formation in turbulent diffusion flames, Chemosphere 42 (2001) 811–821.
[27] C.K. Law, Comprehensive description of chemistry in combustion modeling, Combust. Sci. Technol. 177 (2005) 845–870.
[28] O. Gicquel, N. Darabiha, D. Thévenin, Laminar premixed hydrogen/air counterflow flame simulations using flame prolongation of ILDM with differential diffusion, Proc. Combust. Inst. 28 (2000) 1901–1908.
[29] U. Maas, S.B. Pope, Simplifying chemical kinetics: intrinsic low-dimensional manifolds in composition space, Combust. Flame 88 (1992) 239–264.
[30] B. Fiorina, R. Vicquelin, P. Auzillon, N. Darabiha, O. Gicquel, D. Veynante, A filtered tabulated chemistry model for LES of premixed combustion, Combust. Flame 157 (2010) 465–475.
[31] R. Vicquelin, B. Fiorina, N. Darabiha, O. Gicquel, D. Veynante, Coupling tabulated chemistry with large eddy simulation of turbulent reactive flows, C. R. Mec. 337 (2009) 329–339.
[32] I.M. Kennedy, W. Kollmann, J.-Y. Chen, A model for soot formation in a laminar diffusion flame, Combust. Flame 81 (1990) 73–85.
[33] C.W. Lautenberger, J.L. de Ris, N.A. Dembsey, J.R. Barnett, H.R. Baum, A simplified model for soot formation and oxidation in CFD simulation of non-premixed hydrocarbon flames, Fire Safety J. 40 (2005) 141–176.
[34] J.B. Moss, Modelling soot formation for turbulent flame prediction, in: H. Bockhorn (Ed.), Soot Formation in Combustion: Mechanisms and Models, Springer-Verlag, New York, 1994, pp. 551–568.
[35] B.F. Magnussen, B.H. Hjertager, On mathematical modeling of turbulent combustion with special emphasis on soot formation and combustion, Symp. (Int.) Combust. 16 (1977) 719–729.
[36] R. Said, A. Garo, R. Borghi, Soot formation modeling for turbulent flames, Combust. Flame 108 (1997) 71–86.
[37] A. Refloch, B. Courbet, A. Murrone, P. Villedieu, C. Laurent, P. Gilbank, J. Troyes, L. Tessé, G. Chaineray, J.B. Dargaud, E. Quémerais, F. Vuillot, CEDRE software, 2011, http://www.aerospacelab-journal.org.
[38] J. Galpin, A. Naudin, L. Vervisch, C. Angelberger, O. Colin, P. Domingo, Large-eddy simulation of a fuel-lean premixed turbulent swirl-burner, Combust. Flame 155 (2008) 247–266.
[39] J. Savre, N. Bertier, Y. D'Angelo, D. Gaffié, A chemical time scale approach for FPI modeling, C. R. Mec. 336 (2008) 807–812.
[40] R.J. Kee, J.F. Grcar, M. Smooke, J.A. Miller, A Fortran program for modeling steady laminar one-dimensional premixed flame, Tech. Rep. SAND85-8240, Sandia National Laboratories, 1985.
[41] B. Fiorina, R. Baron, O. Gicquel, D. Thevenin, S. Carpentier, N. Darabiha, Modelling non-adiabatic partially premixed flames using flame-prolongation of ILDM, Combust. Theor. Model. 7 (2003) 449–470.
[42] H. El-Asrag, S. Menon, Large eddy simulation of soot formation in a turbulent non-premixed jet flame, Combust. Flame 156 (2009) 385–395.
[43] G. Ma, J.Z. Wen, M.F. Lightstone, M.J. Thomson, Optimization of soot modeling in turbulent nonpremixed ethylene/air jet flames, Combust. Sci. Technol. 177 (2005) 1567–1602.
[44] D.O. Lignell, J.H. Chen, P.J. Smith, T. Lu, C.K. Law, The effect of flame structure on soot formation and transport in turbulent nonpremixed flames using direct numerical simulation, Combust. Flame 151 (2007) 2–28.
[45] M. Frenklach, H. Wang, Detailed mechanism and modeling of soot particle formation, in: H. Bockhorn (Ed.), Soot Formation in Combustion: Mechanisms and Models, Springer-Verlag, New York, 1994, pp. 165–192.
[46] S.J. Harris, A.M. Weiner, Chemical kinetics of soot particle growth, Ann. Rev. Phys. Chem. 36 (1985) 31–52.
[47] F. Liu, K.A. Thomson, H. Guo, G.J. Smallwood, Numerical and experimental study of an axisymmetric coflow laminar methane–air diffusion flame at pressures between 5 and 40 atmospheres, Combust. Flame 146 (2006) 456–471.

[48] F. Liu, H. Guo, G.J. Smallwood, Ömer L. Gülder, Effects of gas and soot radiation on soot formation in a coflow laminar ethylene diffusion flame, J. Quant. Spectrosc. Radiat. Transfer 73 (2002) 409–421.
[49] M. Fairweather, W.P. Jones, H.S. Ledin, R.P. Lindstedt, Predictions of soot formation in turbulent, non-premixed propane flames, Symp. (Int.) Combust. 24 (1992) 1067–1074.
[50] F. Xu, P.B. Sunderland, G.M. Faeth, Soot formation in laminar premixed ethylene/air flames at atmospheric pressure, Combust. Flame 108 (1997) 471–493.
[51] C.P. Arana, M. Pontoni, S. Sen, I.K. Puri, Field measurements of soot volume fractions in laminar partially premixed coflow ethylene/air flames, Combust. Flame 138 (2004) 362–372.
[52] O.A. Ezekoye, Z. Zhang, Soot oxidation and agglomeration modeling in a microgravity diffusion flame, Combust. Flame 110 (1997) 127–139.
[53] A.D. Abid, N. Heinz, E.D. Tolmachoff, D.J. Phares, C.S. Campbell, H. Wang, On evolution of particle size distribution functions of incipient soot in premixed ethylene–oxygen–argon flames, Combust. Flame 154 (2008) 775–788.
[54] B. Öktem, M.P. Tolocka, B. Zhao, H. Wang, M.V. Johnston, Chemical species associated with the early stage of soot growth in a laminar premixed ethylene–oxygen–argon flame, Combust. Flame 142 (2005) 364–373.
[55] L. Tessé, F. Dupoirieux, B. Zamuner, J. Taine, Radiative transfer in real gases using reciprocal and forward Monte Carlo methods and a correlated-k approach, Int. J. Heat Mass Transfer 45 (2002) 2797–2814.
[56] L. Tessé, F. Dupoirieux, J. Taine, Monte Carlo modeling of radiative transfer in a turbulent sooty flame, Int. J. Heat Mass Transfer 47 (2004) 555–572.
[57] V. Eymet, A.M. Brasil, M. El Hafi, T.L. Farias, P.J. Coelho, Numerical investigation of the effect of soot aggregation on the radiative properties in the infrared region and radiative heat transfer, J. Quant. Spectrosc. Radiat. Transfer 74 (2002) 697–718.
[58] R.S. Mehta, D.C. Haworth, M.F. Modest, An assessment of gas-phase reaction mechanisms and soot models for laminar atmospheric-pressure ethylene–air flames, Proc. Combust. Inst. 32 (2009) 1327–1334.
[59] B. Zhao, Z. Yang, J. Wang, M.V. Johnston, H. Wang, Analysis of soot nanoparticles in a laminar premixed ethylene flame by scanning mobility particle sizer, Aerosol Sci. Technol. 37 (2003) 611–620.
[60] B. Zhao, Z. Yang, M.V. Johnston, H. Wang, A.S. Wexler, M. Balthasar, M. Kraft, Measurement and numerical simulation of soot particle size distribution functions in a laminar premixed ethylene–oxygen–argon flame, Combust. Flame 133 (2003) 173–188.
[61] Z. Qin, V.V. Lissianski, H. Yang, W.C. Gardiner, S.G. Davis, H. Wang, Combustion chemistry of propane: a case study of detailed reaction mechanism optimization, Proc. Combust. Inst. 28 (2000) 1663–1669.
[62] T.J. Poinsot, S.K. Lele, Boundary conditions for direct simulations of compressible viscous flows, J. Comput. Phys. 101 (1992) 104–129.
[63] P.A. Tesner, T.D. Smegiriova, V.G. Knorre, Kinetics of dispersed carbon formation, Combust. Flame 17 (1971) 253–260.
[64] J. Singh, R.I.A. Patterson, M. Kraft, H. Wang, Numerical simulation and sensitivity analysis of detailed soot particle size distribution in laminar premixed ethylene flames, Combust. Flame 145 (2006) 117–127.
[65] A.D. Abid, E.D. Tolmachoff, D.J. Phares, H. Wang, Y. Liu, A. Laskin, Size distribution and morphology of nascent soot in premixed ethylene flames with and without benzene doping, Proc. Combust. Inst. 32 (2009) 681–688.
[66] C.A. Echavarria, A.F. Sarofim, J.S. Lighty, A. D'Anna, Modeling and measurements of size distributions in premixed ethylene and benzene flames, Proc. Combust. Inst. 32 (2009) 705–711.
[67] C.S. McEnally, L.D. Pfefferle, B. Atakan, K. Kohse-Höinghaus, Studies of aromatic hydrocarbon formation mechanisms in flames: progress towards closing the fuel gap, Prog. Energy Combust. Sci. 32 (2006) 247–294.
[68] K.B. Lee, M.W. Thring, J.M. Beér, On the rate of combustion of soot in a laminar soot flame, Combust. Flame 6 (1962) 137–145.
[69] D. Bradley, G. Dixon-Lewis, S.E. din Habik, E.M.J. Mushi, The oxidation of graphite powder in flame reaction zones, Proc. Combust. Inst. 20 (1985) 931–940.